Statistical-mechanical liquid theories reproduce anomalous thermodynamic properties of explicit two-dimensional water models

Peter Ogrin and Tomaz Urbic*
Faculty of Chemistry and Chemical Technology, University of Ljubljana, Vecna Pot 113, SI-1000 Ljubljana, Slovenia

Christopher J. Fennell
Department of Chemistry, Oklahoma State University, Stillwater, Oklahoma 74078, United States

(Received 18 June 2022; accepted 12 August 2022; published 8 September 2022)

We have developed an analytical theory for a simple model of liquid water. We apply Wertheim's thermodynamic perturbation theory (TPT) and integral equation theory (IET) for associative liquids to the rose model, which is among the simplest models of water. The particles interact through rose potentials for orientation dependent pairwise interactions. Modifying both the shape and range of a three-petal rose function, we construct an efficient and dynamical mimic of the two-dimensional (2D) Mercedes-Benz (MB) water model. The particles in 2D MB are 2D Lennard–Jones disks with three hydrogen bonding arms arranged symmetrically, resembling the Mercedes-Benz logo. Both models qualitatively predict both the anomalous properties of pure water and the anomalous solvation thermodynamics of nonpolar molecules. The IET is based on the orientationally averaged version of the Ornstein-Zernike equation. This is one of the main approximations in the present work. IET correctly predicts the pair correlation functions at high temperatures. Both TPT and IET are in semi-quantitative agreement with the Monte Carlo values of the molar volume, isothermal compressibility, thermal expansion coefficient, and heat capacity. A major advantage of these theories is that they require orders of magnitude less computer time than the Monte Carlo simulations.

DOI: 10.1103/PhysRevE.106.034115

I. INTRODUCTION

Water is a critical component in living and industrial systems. From the self assembly of lipid structures in cell walls, to the folding of proteins, to the transport of ions in batteries, water provides the framework for complex molecular scale to macroscopically relevant processes. An accurate treatment of water is necessary to model the chemistry and physics of such systems, and despite its seeming simplicity, water has posed a challenge to treat in a both detailed and efficient manner. Much of this challenge comes down to capturing the strong and highly directional hydrogen bonding interactions that form the network of the liquid and solid states. This strong local ordering has a distant reach and leads to the anomalous properties that are signature to the identity and behavior of water. These anomalous properties principally include the temperature of maximum density at 4 °C, the negative thermal expansion coefficient below this temperature, and the very high liquid state heat capacity [1].

Development of models for water that capture these anomalous properties has often been coupled with an increase in complexity [2]. The widely used atomically realistic models, the SPC [3] and TIP [4] models, have been tuned to generate a variety of explicit water potentials that uniquely capture its dynamic and thermodynamic properties. This often includes the addition of charge and multipolar sites both on and off the oxygen and hydrogen atom centers, such as in the various forms of TIP4P, TIP5P, AMOEBA, and others [5–8]. Increasing complexity is not the only route to capturing water's properties, as there are simpler models that lack atomic details, such as Bol's model [9], the model proposed by Smith and Nezbeda [10,11], and the original Mercedes-Benz (MB) model [12]. The MB water model is a two-dimensional (2D) water model, where molecules are modelled as Lennard–Jones disks with three added arms for hydrogen bond formation. The major advantages of 2D models are computational efficiency and their intuitive form. For such models thermodynamic properties can be calculated with computer simulations in very short amounts of time enabling the underling physical principles to be more extensively explored and clearly visualized than in three-dimensional models. Two-dimensional model simulations have been shown to qualitatively predict the anomalous properties of water and they have been successfully extended to capture thermodynamic properties of solvation of nonpolar solutes [13–19]. The dimensional simplicity of a 2D model makes it an ideal platform for building and refining analytical methods such as thermodynamic perturbation theory, integral equation theory, and general statistical mechanic modeling [20–28]. Such analytical models, along with Monte Carlo (MC) simulations, have recently been extended to successfully investigate how the rotational and translational degrees of freedom independently influence the structural and thermodynamic properties of waters [29–32].

The rose water model is another 2D model that was recently proposed as mimic of MB water model [33]. Similar to the MB model, rose waters are modeled as Lennard–Jones

*tomaz.urbic@fkkt.uni-lj.si

disks with an added hydrogen bonding potential. Instead of Gaussian functions intrinsic to the MB model, sinusoidal functions in polar coordinates, known as rose functions, are used to model the hydrogen bonding interaction. In the case of water a three-petal rose function is used; however, the model is easily adaptable to different orientational interactions, similar to those explored in the original 2D model study from Ben-Naim [12]. With molecular dynamics (MD) simulations, the authors have shown that rose model exhibits the same anomalous properties as the MB model [33]. The advantage of rose model is that it is simpler, computationally more efficient, and the form of the model enables straightforward calculation of forces and torques needed in MD simulation.

While many of the computational investigations of liquid systems resort to either MC or MD using targeted models, these do come with an often significant computational cost. Analytical theories are often significantly faster than MC and MD sampling, and they are often able to determine state dependent properties of a given model that would be difficult to determine with numerical sampling. Some example analytical theories include thermodynamic perturbation theory (TPT) and integral equation theory (IET). A theory has been developed by Wertheim for fluids comprised of molecules that associate into dimers and higher clusters due to the presence of highly directional attractive forces [34,35]. This theory has been successfully applied to a number of different three-dimensional fluid systems, including water and aqueous solutions (see, for example, [11,36,37] and references therein). In the present work, we apply two variants of the theory of associating fluids: the Wertheim's thermodynamic perturbation theory (TPT) [34,35,38,39], and the Wertheim's integral equation theory (IET) [34,40,41]. Both enable calculation of thermodynamic properties, though TPT is generally simpler to use than IET. If structural properties are of interest, the more complex IET is needed. Wertheim's theory is used to model fluids composed of molecules with highly directional attractive forces that can associate in dimers and more complex clusters. Wertheim developed versions of TPT and IET out of the original associating theory.

Wertheim's theory has been successfully applied to a number of different systems, including MB water and general aqueous solutions [20–26]. For the MB model TPT and IET generally work well at high temperatures, however at low temperatures they are less successful. Both theories semi-quantitatively predict molar volume, isothermal compressibility, thermal expansion coefficient and heat capacity [20], and they predict thermodynamic and structural properties of solvation of nonpolar solutes [21]. The rose water model exists in two forms, one modeled to mimic MB water properties and another to more closely reproduce real water's property trends, and this presents a unique opportunity to explore IET and TPT sensitivity. In this study, Wertheim's IET and TPT, previously used for the MB water model, are applied to the two variations of the rose water model. Using these theories, different thermodynamic and structural properties of the rose models are calculated and these results are compared to results from MC simulations. This has the potential to highlight clearly the current strengths and limitations of the IET and TPT approaches.

The paper is organized in following way. The next section the models used in this study are introduced, interaction potentials of MB water model (Sec. II A) and rose water model (Sec. II B) are presented. In Sec. III details of integral equation theory (Sec. III B), thermodynamic perturbation theory (Sec. III C) and the Monte Carlo simulations (Sec. III A) are provided. The results are shown and discussed in Sec. IV and summarized in Sec. V.

II. THE MODELS

A. MB water model

In the MB water model molecules are modeled as two-dimensional Lennard–Jones (LJ) disks, and each disk has three arms attached which can form hydrogen bonds with arms from other molecules [12,13]. Arms are evenly placed on the disk thus the angle between two arms is 120°. All three arms are equivalent. The interaction energy between two MB particles is the sum of the LJ term and hydrogen bonding (HB) term:

$$U(\overrightarrow{X_i}, \overrightarrow{X_j}) = U_{\mathrm{LJ}}(r_{ij}) + U_{\mathrm{H\,B}}(\overrightarrow{X_i}, \overrightarrow{X_j}). \tag{1}$$

$\overrightarrow{X_i}$ is the vector of the position and orientation of the ith particle. The LJ term is calculated in a standard way as

$$U_{\mathrm{LJ}}(r_{ij}) = 4\varepsilon_{\mathrm{LJ}}\left[\left(\frac{\sigma_{\mathrm{LJ}}}{r_{ij}}\right)^{12} - \left(\frac{\sigma_{\mathrm{LJ}}}{r_{ij}}\right)^{6}\right], \tag{2}$$

where $\varepsilon_{\mathrm{LJ}}$ is the depth of the LJ potential and σ_{LJ} is the contact distance. The HB term is a sum of all interactions U_{HB}^{kl} between the arms k and l of molecules i and j, respectively:

$$U_{\mathrm{HB}}(\vec{X}_i, \vec{X}_j) = \sum_{k,l=1}^{3} U_{\mathrm{HB}}^{kl}(r_{ij}, \theta_i, \theta_j). \tag{3}$$

The interaction between two arms is calculated using Gaussian functions which depend on orientation of each interacting molecule and distance between them:

$$\begin{aligned} &U_{\mathrm{HB}}^{kl}(r_{ij}, \theta_i, \theta_j) \\ &\quad = \varepsilon_{\mathrm{HB}} G(r_{ij} - r_{\mathrm{HB}}) G(\vec{i}_k \vec{u_{ij}} - 1) G(\vec{j}_l \vec{u_{ij}} + 1) \\ &\quad = \varepsilon_{\mathrm{HB}} G(r_{ij} - r_{\mathrm{HB}}) G\left\{\cos\left[\theta_i + \frac{2\pi}{3}(k-1)\right] - 1\right\} \\ &\qquad \times G\left\{\cos\left[\theta_j + \frac{2\pi}{3}(l-1)\right] + 1\right\}, \end{aligned} \tag{4}$$

where $G(x)$ is an unnormalized Gaussian function:

$$G(x) = \exp\left(-\frac{x^2}{2\sigma^2}\right), \tag{5}$$

$\varepsilon_{\mathrm{HB}}$ is the HB energy parameter and r_{HB} is the HB distance. $\overrightarrow{u_{ij}}$ is the unit vector in the direction of $\overrightarrow{r_{ij}}$, $\overrightarrow{i_k}$ is the unit vector of the kth arm of the ith particle, and θ_i represents the orientation of ith particle. The interaction between two HB arms is the strongest when distance between the particles is r_{HB} and the interacting arms are parallel and pointing towards each other's centers. Similar to previous studies, energies were expressed in $|\varepsilon_{\mathrm{HB}}|$ and lengths in r_{HB}. HB energy parameter, $\varepsilon_{\mathrm{HB}}$, thus

equals −1 and HB distance r_{HB} is 1. Parameters used in the LJ potential were set to $\varepsilon_{\mathrm{LJ}} = 0.1|\varepsilon_{\mathrm{HB}}|$ and $\sigma_{\mathrm{LJ}} = 0.7 r_{\mathrm{HB}}$.

B. Rose water model

The rose water model is a simple two-dimensional model that mimics the MB water model [33]. The name of the model comes from the use of a polar coordinate rose function to model the orientational HB interaction. Rose functions are sinusoidal functions of the form

$$r = a\sin(n\theta) \text{ or } r = a\cos(n\theta), \tag{6}$$

where n is the number of periods and a is the amplitude of function. Cosine or sine forms of the function are equivalent, with the only difference being a slight rotational offset. Using different combinations of sine (or cosine) functions, functions with different shapes can be produced:

$$r = \sum_{i=1}^{M} a_i \sin^i(n_i\theta). \tag{7}$$

In the case of the rose water model, the number of periods is $n_i = 3$, which gives a three-petal function. As in MB model, molecules are modeled as LJ disks with an added HB potential:

$$U(\vec{X}_i, \vec{X}_j)_{\mathrm{rose}} = U_{\mathrm{LJ}}(r_{ij}) + U_{\mathrm{HB}}(\vec{X}_i, \vec{X}_j), \tag{8}$$

where r_{ij} is distance between centers of molecules i and j, and $\vec{X}_i$ and $\vec{X}_j$ are vectors describing positions and orientations of molecules i and j. The LJ term is the same as in MB water model:

$$U_{\mathrm{LJ}}(r_{ij}) = 4\epsilon_{\mathrm{LJ}}\left[\left(\frac{\sigma_{LJ}}{r_{ij}}\right)^{12} - \left(\frac{\sigma_{LJ}}{r_{ij}}\right)^{6}\right]. \tag{9}$$

The main difference between the rose water model and MB water model is the HB term. In the MB water model, the interaction between two molecules depends on the orientation of both molecules, and as such, the joint pair of particles contributes a single U_{HB} energy. In the rose water model, the contributions of each particle to the HB are separated. This means that the contribution of particle i to the HB is independent of orientation of particle j:

$$U_{\mathrm{HB}}(\vec{X}_i, \vec{X}_j) = U_{\mathrm{HB}}(\vec{r_{ij}}) + U_{\mathrm{HB}}(\vec{r_{ji}}). \tag{10}$$

As result, it is possible that one particle in the interaction forms a half-strength HB with the other, while the other particle does not form an HB interaction with the first particle. Contribution of particle i to the energy of the HB between particles i and j depends on the distance between interacting particles and on the position of particle j in the body frame of particle i. The HB energy contribution of particle i is the product of a distance-dependent term $[s(r_{ij})]$ and orientation-dependent term $[U(\theta_{ij})]$:

$$U_{\mathrm{HB}}(\vec{r_{ij}}) = \frac{\epsilon_{\mathrm{HB}}}{2} * s(r_{ij}) * U(\theta_{ij}), \tag{11}$$

where $\vec{r_{ij}}$ is the vector between particle i and j oriented in body frame of particle i, r_{ij} is the magnitude of this vector, θ_{ij} is the angle of orientation of the vector in the body frame of particle i, and ϵ_{HB} is the HB energy parameter. Due to the fact that $U_{\mathrm{HB}}(\vec{r_{ij}})$ is only half of the HB potential [the other half is $U_{\mathrm{HB}}(\vec{r_{ji}})$], $\frac{1}{2}$ is used in Eq. (11). In the orientation-dependent term of the rose function, the value depends on position of molecule j in body frame of molecule i, in other words it depends on the orientation of molecule i respective to a line between centers of interacting molecules. In the case of rose water model, the orientation-dependent term is

$$U(\theta_{ij}) = a_2 \sin^2(3\theta_{ij}) + a_1 \sin(3\theta_{ij}), \tag{12}$$

where a_1 and a_2 are coefficients that define the amplitude of each sinusoidal term and thus determine the shape of orientational part of the potential. In some cases, use of cartesian coordinates instead of polar coordinates is more convenient. In cartesian coordinates,

$$\sin(\theta_{ij}) = \frac{3x_{ij}^2 y_{ij} - y_{ij}^3}{r_{ij}^3}, \tag{13}$$

where $r_{ij} = \sqrt{x_{ij}^2 + y_{ij}^2}$, x_{ij} and y_{ij} are coordinates of molecule j in cartesian coordinate system of molecule i body frame. Thus, the HB contribution of molecule i in cartesian coordinates is

$$U_{\mathrm{HB}}(\vec{r_{ij}}) = \frac{\epsilon_{\mathrm{HB}}}{2} * s(r_{ij}) * \left[a_2 * \frac{\left(3x_{ij}^2 y_{ij} - y_{ij}^3\right)^2}{r_{ij}^6} + a_1 * \frac{3x_{ij}^2 y_{ij} - y_{ij}^3}{r_{ij}^3} \right]. \tag{14}$$

To incorporate a distance-dependence to the HB interaction, a double-sided cubic switching function, $s(r_{ij})$, is used:

$$s(r_{ij}) = \begin{cases} 0, & r_{ij} < r_l, \\ \frac{(r_l + 2r_{ij} - 3r_{\mathrm{HB}})(r_l - r_{ij})^2}{(r_l - r_{\mathrm{HB}})^3}, & r_l \leqslant r_{ij} < r_{\mathrm{HB}}, \\ \frac{(r_u + 2r_{ij} - 3r_{\mathrm{HB}})(r_u - r_{ij})^2}{(r_u - r_{\mathrm{HB}})^3}, & r_{\mathrm{HB}} \leqslant r_{ij} < r_u, \\ 0, & r_u \leqslant r_{ij}, \end{cases}$$

where r_{HB} is the HB distance, and r_l and r_u are lower and upper bound distance for activation/deactivation of the HB potential. The switching function is symmetrical thus $|r_{\mathrm{HB}} - r_l| = |r_{\mathrm{HB}} - r_u| = r_{\mathrm{FWHM}}$, where r_{FWHM} is "full width at half maximum" of the peak formed by the function. This function is more efficient to compute than the Gaussian functions used in the MB water model, and the parameters of switching function are selected in such a way that the function resembles a Gaussian function.

To summarize, the parameters of rose water model that can be varied are: ϵ_{LJ}, σ_{LJ}, ϵ_{HB}, r_{HB}, r_{FWHM}, a_1, and a_2. Two different sets of these parameters were used in our calculations. One set produces results similar to the MB water model and is here referred to as the MB parametrization, and the other set produces results resembling more experimental-like water and is here referred to as the real parametrization. The MB parametrization values are as follows: $\epsilon_{\mathrm{LJ}} = 0.1$, $\sigma_{\mathrm{LJ}} = 0.7$, $\epsilon_{\mathrm{HB}} = 1$, $r_{\mathrm{HB}} = 1$, $r_{\mathrm{FWHM}} = 0.2$, $a_1 = 0.6$, and $a_2 = -0.4$. The LJ parameters are the same as in MB water model, while the other parameter are chosen in a way that makes the thermodynamic properties of the rose water model similar to those of the MB water model [33].

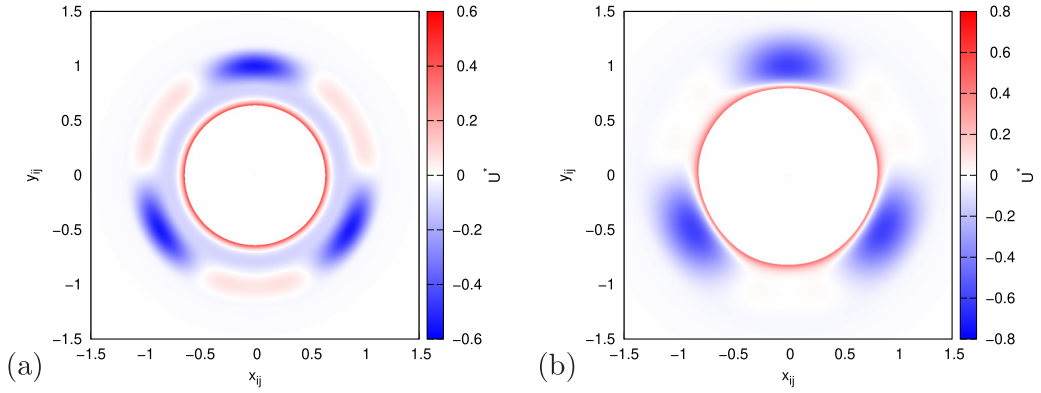

FIG. 1. The combined LJ and HB potential energy surface of the rose water model is similar in form to the three-armed potential of the MB water model. Comparing the potential surface of one rose water particle with the (a) MB parametrization with the (b) real parametrization shows a gap in the MB parametrization between the HB minima and the interior repulsive LJ wall. This separation can lead to stabilizing a dense and orientationally disordered form.

In Fig. 1(a) the potential surface of one rose model molecule with the MB parametrization is shown. The blue color represents favorable interactions and the red color represents unfavorable interactions. There are three regions of highly attractive interaction and between them there are three regions of repulsive interaction. The absolute value of energy at attractive regions is larger than absolute value of energy at repulsive regions. Toward the center of the molecule there is highly repulsive "wall" which is the repulsive portion of the LJ interaction potential that prevents particle overlap.

To obtain more realistic waterlike properties, two major changes of the rose water model are made. The LJ energy parameter is increased to 1/5 of the HB energy parameter and the minimum of the LJ potential is set to coincide with the r_{HB} distance [33]. The width of the HB (r_{FWHM}) is also increased. An accounting of the values of the real parametrization parameters are as follows: $\epsilon_{\mathrm{LJ}} = 0.2$, $\sigma_{\mathrm{LJ}} = 2^{-1/6} r_{\mathrm{HB}}$, $\epsilon_{\mathrm{HB}} = 1$, $r_{\mathrm{HB}} = 1$, $r_{\mathrm{FWHM}} = 5/12$, $a_1 = 0.6$, $a_2 = -0.4$. Figure 1(b) shows the potential surface of one rose water particle with the real parametrization. It is evident in this surface that the repulsive wall of the LJ potential is expanded outward to close the gap between it and the three attractive HB wells seen in the MB parametrization. Moreover, the regions between energetically favorable HB arms are less repulsive, indicating that the real parametrization results in a generally more attractive orientational function.

III. THEORY

A. Monte Carlo simulations

Monte Carlo simulations with the Metropolis algorithm were used to obtain structural and thermodynamic properties of the rose water model using both parametrization schemes. Results from these simulations were used as reference points for comparisons to analytical theories. We were interested in properties of rose water model both at constant volume and constant pressure, therefore simulations were carried out in both the NVT and NpT ensemble. A square basic cell was filled with 100 rose water particles and placed under periodic boundary conditions using the minimum image convention to mimic macroscopic systems. Initial configurations were randomized in both orientation and position with a minimum separation distance of σ_{LJ}. In each simulation step, a molecule was randomly selected for translation or rotation. N translational and N rotational move attempts were performed in each cycle, leading to an average of one translation and one rotation move attempt per particle over the course of each MC cycle. For NpT ensemble simulations, one attempted change of the system volume was included in each cycle. An initial 100 000 cycles were used to equilibrate the systems, and this was followed by 10 individual MC trajectories each sampled for 100 000 cycles. All thermodynamic and structural properties were computed over the course of these production trajectories [13].

B. Integral equation theory

Wertheim's integral equation theory (IET) was applied to both the MB and real parametrizations of the rose water model [34]. In this effort, an orientationally averaged version of the multidensity Ornstein-Zernike (OZ) equation was applied with the polymer Percus-Yevick (PPY) closure [20,34,40,41]. To successfully apply the IET, one additional approximation was made that is not present in MC simulations: the position of bonding arms/regions of a molecule is not fixed. The version of the multidensity OZ equation suitable for use in water models has the following form:

$$\hat{h}(k) = \hat{c}(k) + \hat{c}(k)\rho\hat{h}(k), \tag{15}$$

where $\hat{h}(k)$ and $\hat{c}(k)$ are the matrices with elements that are the Fourier transforms of partial correlation functions $h_{ij}(r)$ and $c_{ij}(r)$. The partial correlation functions used in this OZ equation remain finite with decreasing temperature. A partial density matrix, ρ, was used in Eq. (15) instead of the original Wertheim's density parameters. An ideal network approximation was also used, meaning that the part of correlations that is responsible for forming ringlike structures is neglected [40,41]. Due to the equivalence of the bonding arms, the matrices used in the OZ equation are 2×2-dimensional instead of the traditional 4×4-dimensional form. As such, these

matrices have a structure as follows:

$$\hat{w}(k) = \begin{pmatrix} \hat{w}_{00}(k) & \hat{w}_{01}(k) \\ \hat{w}_{10}(k) & \hat{w}_{11}(k) \end{pmatrix}, \tag{16}$$

where w represents either h or c. The matrix of partial densities is

$$\rho = \begin{pmatrix} \rho & 3\rho \\ 3\rho & 6\rho \end{pmatrix}, \tag{17}$$

where ρ is the average number density of molecules in the system, and coefficients 3 and 6 appear in partial density matrix due to the reduction of dimensionality. To solve the OZ equation, an additional relation that connects h and c correlation functions is needed. Polymer PY closure was used [34]:

$$c_{ij}(r) = f_{\mathrm{LJ}}(r)[t_{ij}(r) + \delta_{i0}\delta_{j0}] + \delta_{i1}\delta_{j1}x^2 \bar{f}_{\mathrm{HB}}(r) e_{\mathrm{LJ}}(r)[t_{00}(r) + 1], \tag{18}$$

where $t(r) = h(r) - c(r)$, x is the fraction of MB particles not bonded at one arm, $f_{\mathrm{LJ}}(r) = e_{\mathrm{LJ}}(r) - 1$, and $e_{\mathrm{LJ}}(r) = \exp[-\beta U_{LJ}(r)]$. $\bar{f}_{\mathrm{HB}}(r)$ is the orientationally averaged Mayer function of the hydrogen bonding potential and is calculated as

$$\bar{f}_{\mathrm{HB}}(r) = \langle \exp[-\beta U_{\mathrm{HB}}(r, \theta_1, \theta_2)] \rangle_{\theta_1, \theta_2} - 1, \tag{19}$$

where $U_{\mathrm{HB}}(r, \theta_1, \theta_2)$ is HB potential of one bonding side. The fraction of particles not bonded at one arm is calculated from mass-action law [34]:

$$x = \frac{1}{1 + 3\rho x \Delta}, \tag{20}$$

where Δ is calculated as

$$\Delta = 2\pi \int g_{00}(r, \rho) \bar{f}_{\mathrm{HB}}(r) r dr. \tag{21}$$

The total radial distribution function (pair distribution function) $g(r)$ was calculated as

$$g(r) = g_{00}(r) + 3g_{01}(r) + 3g_{10}(r) + 9g_{11}(r), \tag{22}$$

where $g_{ij}(r) = h_{ij}(r) + \delta_{i0}\delta_{j0}$ [20]. To solve the OZ equation together with PPY closure, the direct iterative method was used. In addition, the method of Talman was used to carry out forward and inverse Fourier-Bessel transformation [42].

After determination of a pair distribution function, thermodynamic quantities can be calculated using standard thermodynamic relations. The internal energy per particle is calculated as

$$\beta U = 1 + \pi\beta\rho \int_0^\infty U_{\mathrm{LJ}}(r) e_{\mathrm{LJ}}(r) y(r) r dr + 9\beta\pi x^2 \rho \left[\int_0^\infty U_{\mathrm{LJ}}(r) e_{\mathrm{LJ}}(r) \bar{f}_{\mathrm{HB}}(r) y_{00}(r) r dr + \int_0^\infty \langle U_{\mathrm{HB}}(r, \theta_1, \theta_2) \exp[-\beta U_{\mathrm{HB}}(r, \theta_1, \theta_2)] \rangle_{\theta_1, \theta_2} e_{\mathrm{LJ}}(r) y_{00}(r) r dr \right], \tag{23}$$

where $\langle ... \rangle_{\theta_1, \theta_2}$ denotes orientational averaging, $y_{ij}(r)$ is a partial cavity distribution function, which when using PPY is equal to $y_{ij}(r) = g_{ij}(r) - c_{ij}(r)$ [20,43]. The total cavity distribution function is calculated as $y(r) = y_{00}(r) + 3y_{01}(r) + yg_{10}(r) + 9y_{11}(r)$. The pressure is determined via the virial equation [34], which has the following form:

$$p = 1 - \frac{\pi\rho^2}{2} \int_0^\infty \frac{\partial U_{\mathrm{LJ}}(r)}{\partial r} e_{\mathrm{LJ}}(r) y(r) r^2 dr - \frac{9\pi x^2 \rho^2}{2} \left[\int_0^\infty \frac{\partial U_{\mathrm{LJ}}(r)}{\partial r} e_{\mathrm{LJ}}(r) \bar{f}_{\mathrm{HB}}(r) y_{00}(r) r^2 dr + \int_0^\infty \left\langle \frac{\partial U_{\mathrm{HB}}(r, \theta_1, \theta_2)}{\partial r} \exp[-\beta U_{\mathrm{HB}}(r, \theta_1, \theta_2)] \right\rangle_{\theta_1, \theta_2} e_{\mathrm{LJ}}(r) y_{00}(r) r^2 dr \right]. \tag{24}$$

To calculate properties at constant pressure, the bisection method was used to determine the density at which the pressure of the system equals the target pressure. This enabled calculation of thermodynamic quantities at the newly determined density.

C. Thermodynamic perturbation theory

In addition to IET, Wertheim's thermodynamic perturbation theory (TPT) was applied to both parametrizations of the rose water model [34,35]. In TPT, the Helmholtz free energy is the primary quantity calculated, and all other thermodynamic quantities can be determined from it. For MB water and the rose water models, the total Helmholtz free energy of the system, A, is the sum of the LJ and HB terms:

$$\frac{A}{Nk_BT} = \frac{A_{\mathrm{LJ}}}{Nk_BT} + \frac{A_{\mathrm{HB}}}{Nk_BT}, \tag{25}$$

where N is the number of particles, k_B is the Boltzmann constant, and T is the temperature. In this way, hydrogen bonds are considered as a perturbation of the system of LJ disks. The free energy of a system of LJ disks is calculated using Barker-Henderson perturbation theory [20,44–46], where hard disks (HD) are used as a reference system and the LJ potential is used as the perturbation:

$$\frac{A_{\mathrm{LJ}}}{Nk_BT} = \frac{A_{\mathrm{HD}}}{Nk_BT} + \frac{\rho}{2k_BT} \int_{\sigma_{\mathrm{LJ}}}^\infty g_{\mathrm{HD}}(r, \eta) u_{\mathrm{LJ}}(r) d\vec{r}, \tag{26}$$

where A_{HD} is the Helmholtz free energy of hard disks, g_{HD} is the radial distribution function of hard disks, and σ_{LJ} is the LJ contact distance. To calculate free energy of hard disks, the following equation was used [20,47]:

$$\frac{A_{\mathrm{ex,HD}}}{Nk_BT} = -1.10865 - 0.8678\log(1 - \eta) - 0.0157(1 - \eta) + \frac{1.1322}{1 - \eta} - \frac{0.00785}{(1 - \eta)^2}. \tag{27}$$

The key parameter of the HD free energy is the packing fraction, calculated as $\eta = \frac{1}{4}\pi\rho d^2$. The d value is the hard disk diameter, calculated as

$$d = \int_0^{\sigma_{LJ}} \{1 - \exp[-\beta u_{LJ}(r)]\} dr. \tag{28}$$

The radial distribution function of hard disks $g_{HD}(r)$ was calculated using the expression of Gonzalez *et al.* [48].

The Helmholtz free energy of the HB contribution was calculated using

$$\frac{A_{HB}}{Nk_BT} = 3\left(\log x - \frac{x}{2} + \frac{1}{2}\right), \tag{29}$$

where x is the fraction of HB particles not bonded at one arm (the same fraction that was used in IET) [20,34]. This fraction is calculated in the same way as in IET, using the mass-action law:

$$x = \frac{1}{1 + 3\rho x\Delta}, \tag{30}$$

where Δ is defined as

$$\Delta = 2\pi \int g_{LJ}(r, \rho)\bar{f}_{HB}(r) r dr. \tag{31}$$

Here, $\bar{f}_{HB}(r)$ is the same orientationally averaged Mayer function that was used in IET. The radial distribution function needed in Eq. (31) was calculated by solving the Ornstein-Zernike equation with PY closure for the system of LJ disks.

All other thermodynamic quantities were calculated using standard thermodynamic relations [45,49], these following from the determination of the Helmholtz free energy.

IV. RESULTS AND DISCUSSION

All results are presented in reduced units, reduced in relation to the strength and length of an HB interaction. In this reduction, the HB energy parameter ϵ_{HB} was used to normalize temperature and excess internal enthalpy ($A^* = \frac{A}{|\varepsilon_{HB}|}$, $T^* = \frac{k_B * T}{|\varepsilon_{HB}|}$), while all distances were normalized with characteristic length of the hydrogen bond r_{HB} ($r^* = \frac{r}{r_{HB}}$).

A. Structural properties

As the structure of a liquid affects all its thermodynamic properties, changes in a liquid's structure will result in changes in the respective thermodynamic properties. To better understand and explain how changing conditions, such as different temperatures, alter the thermodynamic properties of the system, it is important to uncover how different conditions affect the overall structure of the liquid. As such, structural properties of rose water model were investigated first. Of the two parametrizations of interest, we start with exploring the MB parametrization of the rose water model as it is expected to show strong similarities with results obtained using the original Mercedes-Benz water model [13,15,20].

1. MB parametrization

Figure 2 shows example configurations of rose water model particles in NVT Monte Carlo simulations at various temperatures and density 0.7. Strong interaction contacts between particle pairs, where the interaction energy was less than −0.5, are shown with red lines. These interactions include strong hydrogen bonds and very tight neighbor contacts that are favorable regardless of particle orientation. When the temperature is low, $T^* = 0.1$ in Fig. 2(a), particles in the system are generally highly ordered as the structures observed are mostly crystalline. The open hexagonal packing is apparent at low temperature, visible with the red hexagonal grid that forms in much of the systems. Some particles also adopt structures that are less ordered, forming defects in the overall crystal. When the temperature increases to $T^* = 0.15$ [Fig. 2(b)], near or slightly above the melting temperature of the model [33], the hexagonal structure of the system collapses to a higher density domain that is not as ordered. The network of favorable contacts is looser and less symmetrical at this temperature, indicative of a liquidlike structure. The system at this temperature has properties of liquid state, there is no long-ranged order, but there is still some short-ranged order. Figure 2(c) shows the system at $T^* = 0.2$, which is expected to be a liquid state form at this fixed density. The rose water particles still form favorable pairing contacts, but they fill the free space in a more uniform manner. At this temperature, longer chains of particles connected with favorable interactions are present in the system, and cyclic structures are less apparent than observed at lower temperatures. At a high temperature of $T^* = 0.5$ in Fig. 2(d), the majority of particles interact via chains of different lengths; however, these chains are shorter than the chains generally observed at lower temperatures.

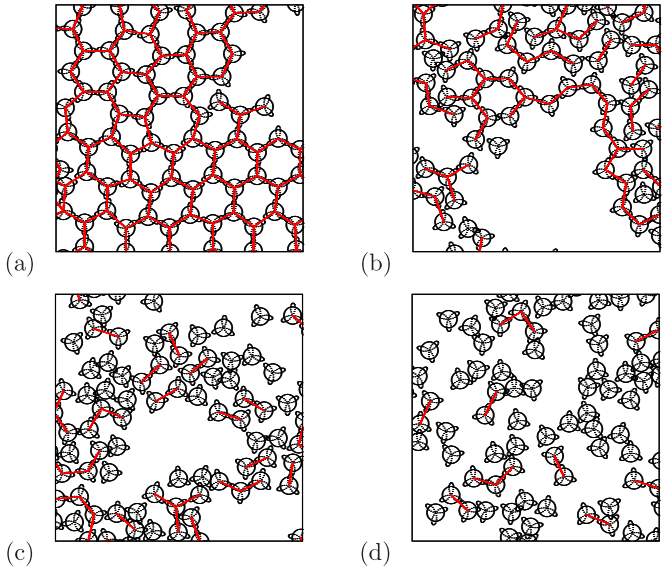

FIG. 2. At low density, the MB parametrization of rose water will readily melt with increasing temperature in NVT simulations. Snapshots are shown for systems with a density of 0.7 and temperatures of: (a) $T^* = 0.1$, (b) $T^* = 0.15$, (c) $T^* = 0.2$, (d) $T^* = 0.5$. The red lines indicate potential hydrogen bond contacts between the black line illustrated representations of rose water molecules.

In Fig. 3, radial distribution functions (RDFs) of water are shown for the rose water model with the MB parametrization alongside the MB water model at a constant pressure

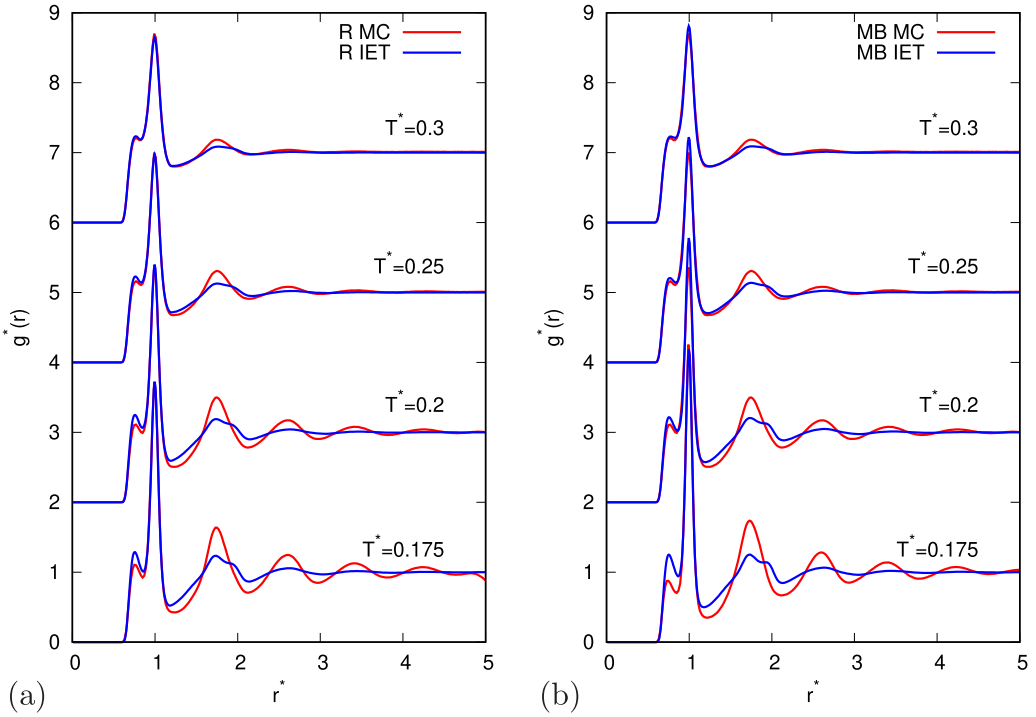

FIG. 3. Water-water radial distribution functions at increasing temperature and a constant pressure of $p^* = 0.12$ shows how increasing disorder at higher temperatures leads to improved agreement between MC simulations (red curves) and IET (blue curves). The stacked $g(r)$ plots are each vertically offset by 2 for comparison and show increasing temperature from 0.175, 0.2, 0.25, and 0.3. The (a) rose water model on the left is consistently less structured than the (b) MB water model on the right.

of $p^* = 0.12$. The RDFs are stacked according to increasing temperatures from $T^* = 0.175$ upwards to $T^* = 0.3$. The red curves show the results from Monte Carlo simulations (MC) while results with IET are blue. Comparing radial distribution functions of both models calculated with MC simulations [Fig. 3(a) with Fig. 3(b)], it is evident that the functions describing both models are very similar, though they differ slightly in the specific height of the RDF peaks. The distance of the first small peak corresponds to the separation distance between two molecules in LJ contact, while the taller second peak correspond to two molecules with potentially a direct hydrogen bond between them. At this pressure, the first small peak of the RDF is noticeably higher in the case of the rose water model at the lower temperatures, and this indicates that the rose water model tends to adopt more disordered states than the MB water model with more molecules in LJ contact. This loss of structure carries over to the second peak, which is lower in the rose water model than the MB water model, indicating a loss in direct HB interactions at the same thermodynamic state point. As the temperature increases, these differences become less and less noticeable with both models assuming less orientationally ordered states.

In both water model cases, IET is quite successful at predicting RDFs, though this agreement is very much temperature dependent. The theory successfully predicts the position of major peaks that appear in the RDFs calculated with MC; however, the amplitude of the peaks calculated with theory differs from the simulations to some extent. The peaks predicted by IET are lower than those calculated with MC, consequently IET predicts a less structured system than MC. The reason for this is orientation averaging present in IET. For both models, the IET prediction of the first two peaks is more accurate than the prediction of more distant peaks. IET is more successful at predicting RDFs in the case of the rose water model than in case in case of MB water model. This is most clearly seen with the amplitude of the first peak being in tighter agreement between IET and the rose water model simulations. As the temperature increases, IET and MC simulations give quite similar results. IET struggles with highly structured liquids, and the loss of strong hydrogen bonding with increased temperature means that orientational interaction approximations in IET are less severe.

Raising the temperature of the simulations increases disorder in these systems, and this has the effect of increasing the similarity of the rose water and MB models. Increasing pressure on a systems where the ordered crystalline form has a lower density than the more disordered higher density form should have a similar effect. Figure 4 shows the same models and temperatures seen in Fig. 3, only the constant pressure has been increased to $p^* = 0.19$. The RDFs look similar at these differing pressures, though the differences do align with favoring states with decreased overall order. This is most easily seen in the relative heights of the first two peaks in all of the RDFs. For example, at the lowest shown temperature of $T^* = 0.175$, the first peak of the rose water model MC simulation curve grows from a $g^*(r)$ value of nearly 1.0 to about 1.2, this while the tall second peak decreases from 3.8 down to 3.5. These combined changes are consistent with favoring more dense and less orientationally ordered states. The RDFs of the rose water and MB water models are also in closer agreement at this higher pressure, particularly when the temperature is also high. While HB interactions are still present as seen in the

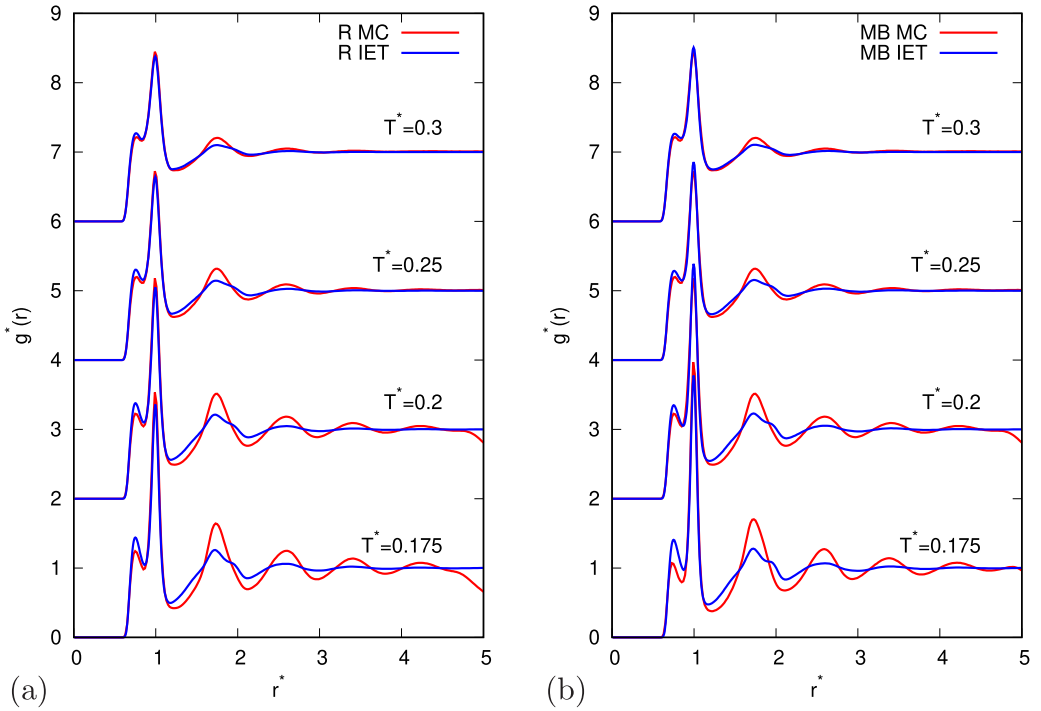

FIG. 4. Water-water radial distribution functions at increasing temperature and a constant pressure of $p^* = 0.19$ shows how increasing disorder at higher temperatures leads to improved agreement with IET. The stacked $g(r)$ plots are each vertically offset by 2 for comparison and show increasing temperature from 0.175, 0.2, 0.25, and 0.3. The (a) rose water model on the left is consistently less structured than the (b) MB water model on the right, and this higher pressure of 0.19 favors more compact and further disordered states than does $p^* = 0.12$ in Fig. 3.

still tall first hydration shell peaks, the specific distinctions in how the HB interactions are calculated become less important at higher pressure. The more orientationally disordered LJ interaction potential is handled identically between the rose water and MB water model, and these LJ interactions tend to dominate at high pressure state points.

This increase in pressure has a small overall effect on the IET curves, though it is one that is similar to that seen in the MC simulations. At higher pressure, the first RDF peak grows taller than that from the IET calculations at lower pressure. All other peaks are dampened, indicating a favoring of more disordered states at all of the temperatures shown. The agreement between IET and MC simulations changes very little, unlike the convergence in behavior seen with increasing temperature. All the peak locations remain consistent between IET and MC simulations, and IET simply becomes more and more accurate at predicting peak and trough magnitudes as the temperature grows.

2. *Real parametrization*

The real parametrization of the rose water model differs from the MB water model by not having a σ_{LJ} parameter that is notably smaller than r_{HB} and by having a modestly wider HB interaction well. Despite these changes, this real parametrization of the rose water model still appears to capture the anomalous property behavior observed in the MB water model, though in ways more attuned to the behavior seen in experiments.

In Fig. 5, example positions and orientations of the real parametrization rose water model particles during Monte

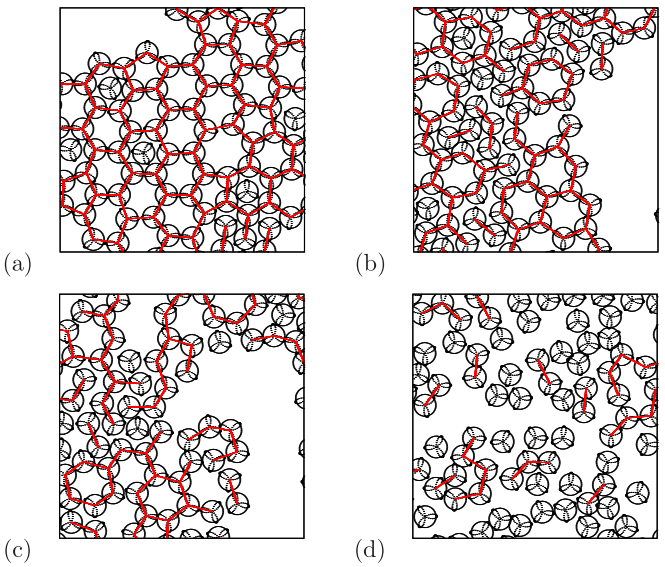

FIG. 5. The real parametrization of rose water behaves similarly to the MB parametrization in that it will readily melt with increasing temperature in NVT simulations. Snapshots are shown for systems with a low density of 0.7 and temperatures of: (a) $T^* = 0.1$, (b) $T^* = 0.15$, (c) $T^* = 0.2$, (d) $T^* = 0.5$. The red lines indicate strong interaction contacts between the illustrated representations of rose water molecules.

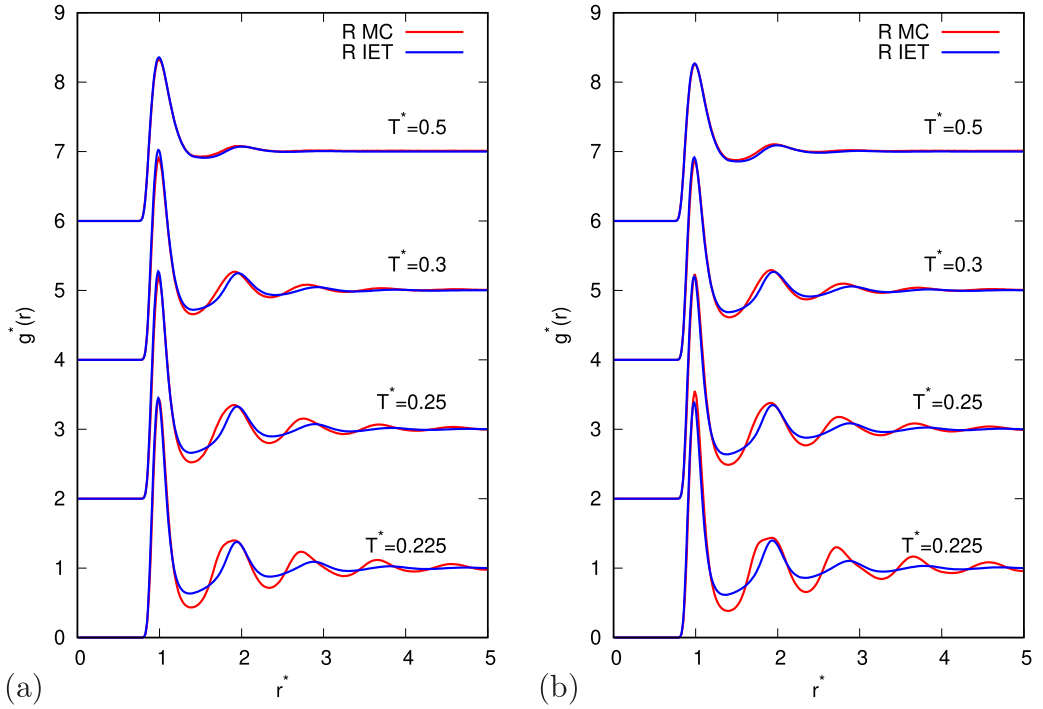

FIG. 6. Water-water radial distribution functions at increasing temperature and a constant pressures of $p^* = 0.12$ (left) and $p^* = 0.19$ (right) shows improved agreement of MC simulations (red curves) with IET calculations (blue curves) with increasing temperature. The stacked $g(r)$ plots are each vertically offset by 2 for comparison and show increasing temperature from 0.225, 0.25, 0.3, and 0.5.

Carlo simulation are shown at various temperatures and constant density of 0.7. With a temperature of $T^* = 0.1$ in Fig. 5(a), a highly ordered structure of molecules connected with strong interactions is formed. Comparing the snapshots see here to those from the MB parametrization in Fig. 2(a), the real parametrization model shows a less ordered structure overall. It appears that pentagon, heptagon, and even octagon arrangements are stabilized in addition to the hexagonal structures primarily seen in the MB parametrization crystals. The reason for this change in ordering is likely due to the wider HB interaction well and the lack of the repulsive orientational potential that penalizes particles that do not adopt hydrogen bonding orientations (see Fig. 1). These differences make the HB interaction more promiscuous in general. As the temperature increases above the melting temperature to 0.15 [Fig. 5(b)], the system loses much of the open crystalline order, forming a more well-packed domain that is less reliant upon specific hydrogen bonding orientations. When the temperature increases further to 0.2 [Fig. 5(c)] some more chainlike structures do appear, as seen in the MB parametrization, though not to the same extent as this latter model. Even though there is a reduction in hydrogen bonds in the system, the particles are still connected with the well-packed cluster. At the highest temperature shown in Fig. 5(d), there is a continued decrease in hydrogen bonds in the system, with a shift from ringlike structures to chainlike structures. This shift is not as dramatic as that seen with the MB parametrization, and the temperature dependence of the interaction behavior is less variable overall.

Radial distribution functions were calculated for the real parametrization of the rose water model as a function of temperature at constant pressures of $p^* = 0.12$ and $p^* = 0.19$ in Fig. 6 using both MC sampling (red curves) and IET (blue curves). The main difference between these RDFs and those of the rose water model with the MB parametrization seen in the previous section is in the first peak(s). In the MB parametrization there is a split first peak. The small initial peak consists of dense packed states that can be more orientationally disordered, while the tall second peak is seen for optimally hydrogen bonded particles. In the real parametrization there is no clear separation of these states as the HB and LJ potentials have consistent minima as a function of radial distance (see Fig. 1), and the MB parametrization has two characteristic size parameters for the interaction minima: r_{HB} for the HB potential and $2^{1/6} \times 0.7 \times r_{\mathrm{HB}}$ for the LJ potential. The single potential minimum distance of r_{HB} in the real parametrization results in a generally less structured system that is more accepting of bent HB interactions, resulting in peaks in the RDFs that are broader with decreased height. As with the other parametrization, this structure decreases with increasing temperature in the stacked plots shown, temperatures that extend up to $T^* = 0.5$ in these comparisons.

IET is even more successful at predicting the RDFs of the rose water model with the real parametrization than the MB parametrization. As with the MB parametrization series, the agreement between the functions calculated with IET and MC improves with increasing temperature. Integral equation theory accurately predicts the position of peaks at all shown temperatures. In general, IET predicts a less structured system than MC as the peaks and troughs predicted by IET are moderately less intense than those calculated by MC. The reason for this improved agreement with the real parametrization of the rose water model comes from the reduced repulsion between unfavorably oriented HB interactions (see Fig. 1),

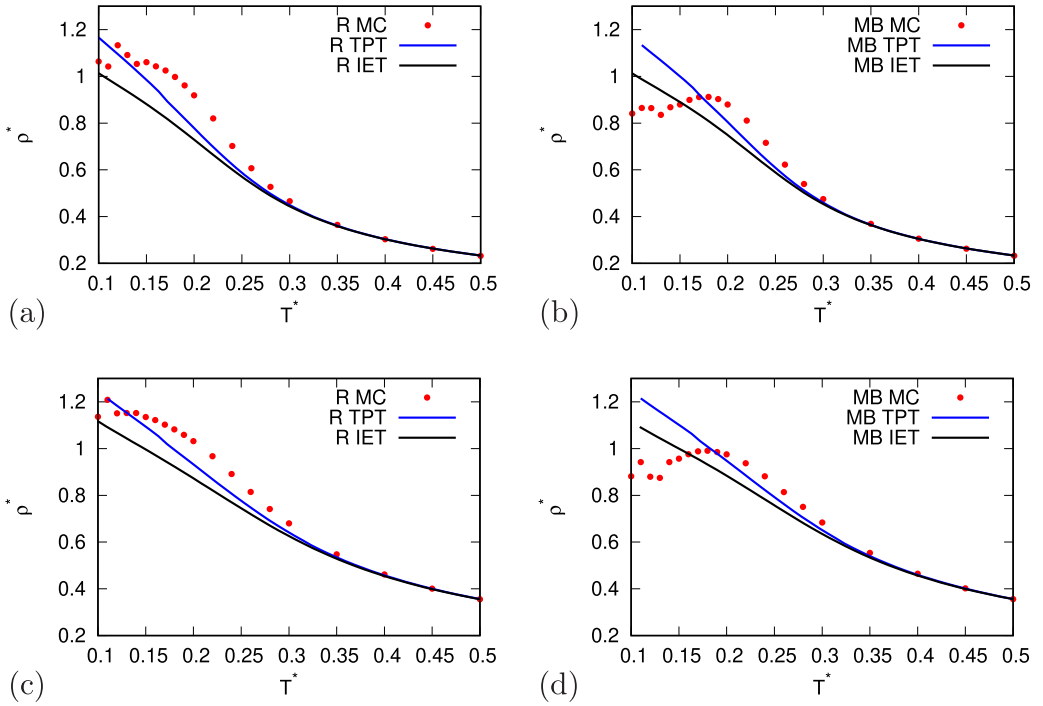

FIG. 7. The MB water model and rose water model with the MB parametrization both show temperature dependent density maxima, though these are not apparent in TPT and IET. The plots shown are of density as function of temperature at constant pressure $p^* = 0.12$ (first row) and $p^* = 0.19$ (second row). Results for the rose water model are in the left column and results for the MB water model are in the right column. The red points show results from MC simulations, while the blue line shows results from TPT and the black line shows results from IET.

leading to a more promiscuous orientational potential. This less selective orientational potential is more consistent with the orientational averaging approximation used in IET, so the error between IET and the real parametrization of the rose water model is reduced.

B. Thermodynamic properties

1. MB parametrization

While the structure of the interaction potential is fundamentally different, it has been indicated that the rose water model is able to reproduce many of the temperature dependent thermodynamic properties exhibited by the MB water model [33]. To explore this capability in more detail, we studied thermodynamic properties of the rose water model with the MB parametrization at constant pressure and compared these to properties of MB water model using MC calculations, IET, and TPT.

Figure 7 shows the density of the rose water model and MB water model as a function of temperature at two constant pressures. It is evident in these panels that the MB water model and the rose water model with the MB parametrization report extremely similar densities at temperatures higher than 0.25 at both of the chosen pressure values. The models do deviate at lower temperatures, with the rose water model generally having a greater density at temperatures near the points of maximum density. This density difference between the models is consistent with the rose water model being less structured than the MB model, as seen in the radial distribution function profiles (Fig. 3). The temperature where this density maximum is observed appears at a lower value for the rose water model than the MB water model, again a likely consequence of the reduced structure of the model.

Thermodynamic perturbation theory and integral equation theory are both successful at predicting density at temperatures above 0.3, showing quantitative agreement in the density values and reproducing well the curvature with increasing temperature. As the temperature decreases below 0.3 both theories do correctly predict an increase in density, though the agreement with MC calculations becomes increasingly poor. Neither TPT nor IET successfully reproduce the point of density maximum observed in the MC calculations. It is clear from the radial distribution function analyses that IET is less structured than the MB water model and both parametrizations of the rose water model. The maximum in the density of water is a consequence of increasing order due to more persistent hydrogen bonding interactions as the temperature lowers. The interactions prefer a lower density expanded state relative to higher density states that lack the orientational ordering of ideal hydrogen bonds. While neither TPT nor IET capture this feature, TPT does a better job at reproducing the density values of MC calculations than does IET. This agreement between MC calculations and both TPT and IET improves with increasing pressure. This likely comes from the fact that increasingly dense states tend to be favored at higher pressures with both the MB water and rose water models, and these states tend to be less structured, which is consistent with the behavior of the analytical theories.

Figures 8 and 9 show the excess enthalpy and entropy respectively as a function of temperature for two different

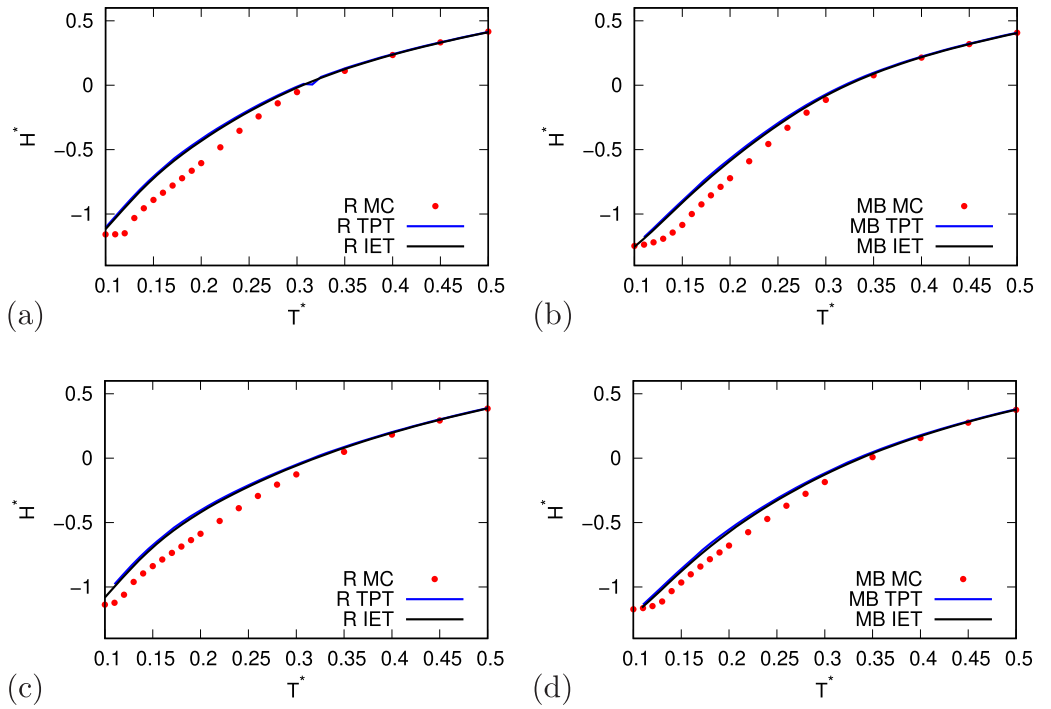

FIG. 8. Excess enthalpy as function of temperature shows similar behavior for rose water and MB water, though the analytical theories tend to better agree with simulation at lower pressures. The plots shown are from calculations at constant pressure $p^* = 0.12$ (first row) and $p^* = 0.19$ (second row) for rose water on the left and MB water on the right. The red points are from MC simulations, while the blue lines show TPT results and the black lines show IET results.

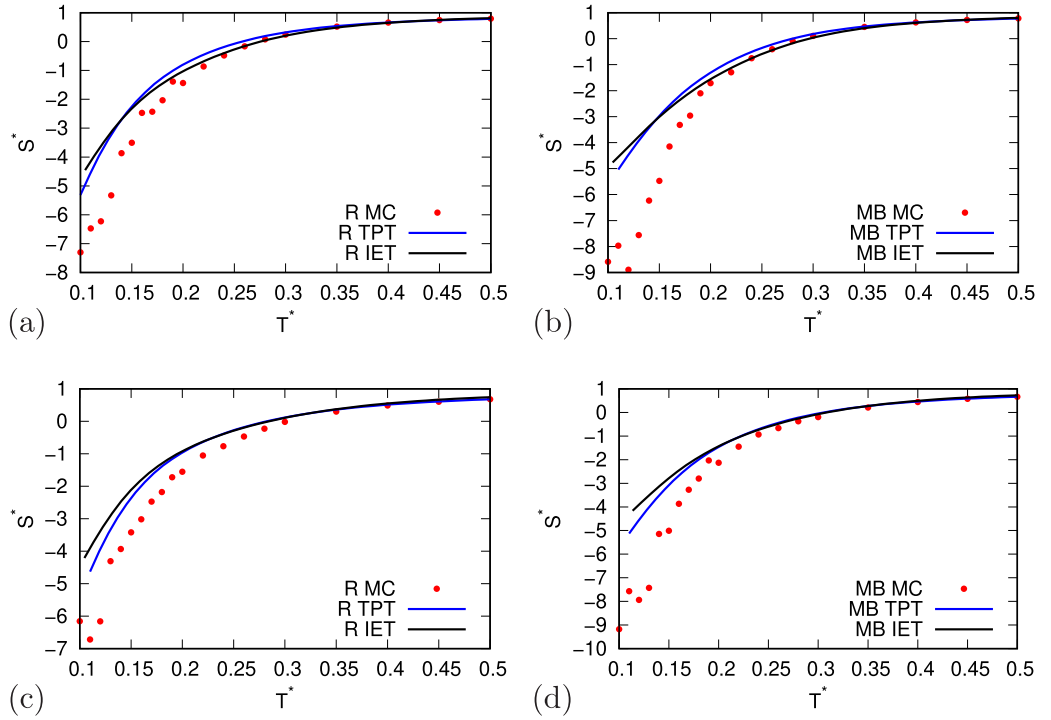

FIG. 9. Excess entropy as function of temperature shows similar behavior for rose water and MB water, though the analytical theories tend to better agree with simulation at lower pressures. The plots shown are from calculations at constant pressure $p^* = 0.12$ (first row) and $p^* = 0.19$ (second row) for rose water on the left and MB water on the right. The red points are from MC simulations, while the blue lines show TPT results and the black lines show IET results.

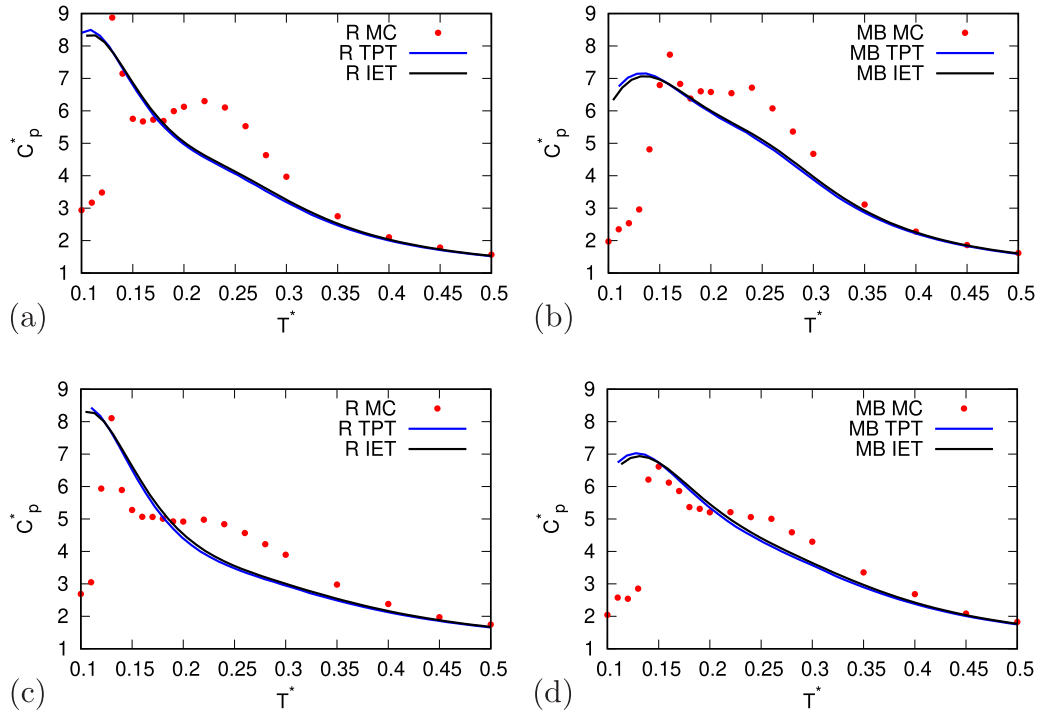

FIG. 10. The change in excess heat capacity as a function of temperature shows elevated values near and above the melting transitions for the rose water model on the left and MB water model on the right. The data shown are from constant pressure $p^* = 0.12$ (top row) and $p^* = 0.19$ (bottom row). The red points are from MC simulations, while the blue lines show TPT results and the black lines show IET results.

pressures. The excess enthalpy and entropy of both water models increases with increasing temperature. The values of the enthalpy and entropy are negative up to a temperature of approximately 0.3 and positive at higher temperatures. At these high temperatures, both rose water and MB water report similar H^* and S^* values, and the TPT and IET theories match as well. This agreement comes about because the contribution of hydrogen bonds to enthalpy and entropy diminishes with increasing temperature, and the subtle details of structuring become less significant. The primary differences between the models and the theories appear at low temperature where the orientational restrictions of hydrogen bonding begin to matter more. While not readily apparent in these plots, the rose water model generally has a higher enthalpy and entropy than MB water at any given low temperature. For example, at $T^* = 0.2$ and $p^* = 0.12$ the rose water model has an excess enthalpy of -0.6 and entropy of -0.3 while the MB water model has values just above -0.8 and -0.6 at this same state point. This difference is consistent with the less rigid structuring of the rose water model. The reason that this difference between models is not readily apparent comes from the difference in curvature of the TPT and IET plots for the rose water and MB water models. The rose water model forms of the theories have a steeper change in curvature than the MB water model forms, noticeable between temperatures of 0.15 and 0.2. This less gradual change in curvature leads to a slightly poorer agreement between the analytical theories and the rose water model than that seen for the analytical forms with the MB water model.

The excess heat capacity, C_p^* as a function of temperature at two different constant pressures is shown in Fig. 10. As with other properties, at high temperatures the rose water and MB water simulation results are highly similar and the differences between the models is more visible at lower temperatures. The notable features present in all these simulation results are the two maxima at lower temperatures. The taller and sharper peak is due to the phase transition from solid to liquid state, while the lower and broader second maximum is due to the high dynamics of hydrogen bonding interactions at that temperature. As with real water, these models show an overall elevated heat capacity in the liquidlike state, the state where there are a large number of fluid hydrogen bonds. This is bracketed by low C_p^* values both at very high temperatures, due to the loss of potential hydrogen bonding interactions with the low density, and at very low temperatures, due to the crystalline structure with persistent hydrogen bonding. Increasing pressure primarily affects the liquid state C_p^* peak by lowering the free space and decreasing the dynamics of hydrogen bond formation and breaking, lowering the C_p. The primary difference between the rose water model and the MB water model is the location of phase transition maximum, which is at a slightly lower temperature in the rose water model.

As with the other thermodynamic properties, IET and TPT are successful at calculating the C_p^* seen in the MC simulations at constant pressure at high temperatures for both models. This success is not seen at low temperatures, with clear differences at temperatures below 0.35. Neither IET or TPT are able to reproduce the second maximum at higher temperatures, and mainly show smooth curves that peak at a temperature below the MC simulation melting peaks of the models at both shown pressures. While the agreement is not strong for any of these cases at low temperatures, it does appear that there is noticeably better agreement for the MB water model versions.

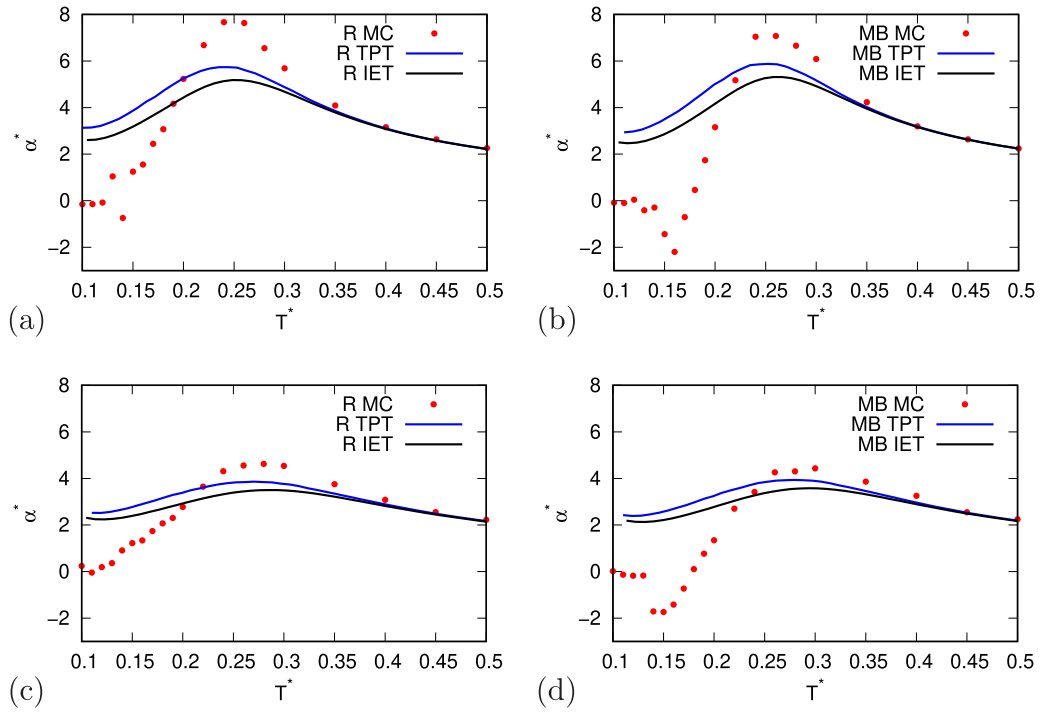

FIG. 11. All models show a maximum in the coefficient of thermal expansion, with the rose water and MB water simulation results showing a characteristic crossing to negative values at the temperature of maximum density. As with other plots, the rose water model is show in the left plots and MB water model on the right plots. The data shown are from constant pressure $p^* = 0.12$ (top row) and $p^* = 0.19$ (bottom row). The red points are from MC simulations, while the blue lines show TPT results and the black lines show IET results.

In Fig. 11 the temperature dependence of the coefficient of thermal expansion is shown at two different pressures. The negative value for the coefficient of thermal expansion below the temperature of maximum density is one of water's well known anomalous properties, and this is seen in the MC simulations of both the rose water model and MB water model. As temperature increases from these values, a maximum is observed between temperatures of 0.25 and 0.3 at these pressures, and the property asymptotically approaches a value of $1/T^*$ as the temperature further increases. The rose water and MB water models have nearly the same maxima locations and values, though differences appear at low temperature. In particular, the rose water model anomalous behavior is less pronounced, and this is consistent with its corresponding shift in the density maximum to lower temperature and an apparent narrowing of the gap between this maximum and the melting point. In both the rose water and MB water models, increasing the pressure lowers the height of the maximum of the coefficient of thermal expansion, which is expected given the reduced free volume under higher pressure conditions.

The agreement between IET and TPT and the respective model simulations is almost perfect for calculation of the expansion coefficient at high temperatures. While this agreement degrades at low temperatures, these analytical theories do predict the coefficient's maximum at the same temperature as the MC simulations, though the magnitude is lower. As with the density results, the expansion coefficient agreement with simulations is slightly better for TPT then for IET, this seen in the higher maxima of the blue curves in Fig. 11. This agreement is modestly better with the MB water model than with the rose water model because of the slightly lower magnitude maximum seen from the MB water model simulations.

The temperature dependence of the isothermal compressibility at two different pressures is shown in Fig. 12. The rose water and MB water models strongly agree with one another with low values at low temperatures and the isothermal compressibility increases to approach $1/p^*$ at high temperatures. This rapid rise increases with a decrease in the number of hydrogen bonds and decrease in the density. Less dense materials are generally more compressible, though the low density solid form of water has a very low compressibility as it is crystalline with a tightly hydrogen bonded network. Of interest in these curves is the liquid state minimum in the isothermal compressibility, which occurs at nearly the same temperature as the point of maximum density. This is a compressibility minimum due to the high density, highly cramped molecular environment. This decrease in compressibility with decrease in free volume of the molecules is generally seen by comparing the results at different pressures. The isothermal compressibility values drop nearly in half in moving from $p^* = 0.12$ to $p^* = 0.19$, and this decrease is seen across nearly the entire temperature range shown for all models.

Both TPT and IET are successful in predicting the key features of how the isothermal compressibility changes with temperature; however, TPT shows a better agreement with MC simulation than IET. This agreement is nearly quantitative at temperatures above 0.25, and it degrades at lower temperatures. Note that the compressibility of the MC simulations drops to nearly zero at very low temperatures, and this corresponds to the transition to a solid phase. As previously mentioned, both TPT and IET are unsuccessful in predicting

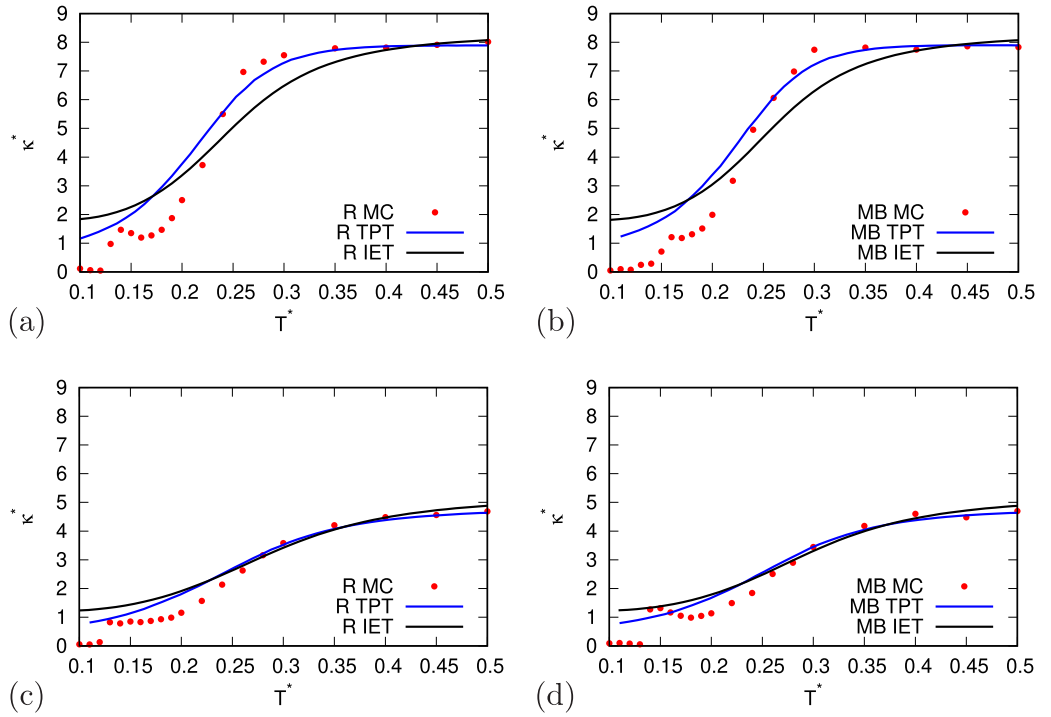

FIG. 12. Isothermal compressibility as function of temperature is comparably well reproduced between the rose water and MB water models, here at constant pressure $p^* = 0.12$ (top row) and $p^* = 0.19$ (bottom row) conditions. The red points are from MC simulations, while the blue lines show TPT results and the black lines show IET results.

properties of solid materials, so it is expected that they will be unable to capture this large drop in the isothermal compressibility. Neither TPT nor IET can reproduce the liquid state minimum in the compressibility, though this is a subtle anomaly in a phase regime were these models struggle.

2. Real parametrization

The real parametrization of the rose water model was developed to explore how flexible these single point potential energy surfaces can be and to clarify what parameters are critical for the reproduction of real water's anomalous properties. The key change, beyond the magnitude of the LJ and HB strength parameters, is to unify the minima of the LJ and HB potentials. This unification means that the density difference between a typical solid form and the liquid state density maximum will be smaller. As discussed in the radial distribution function analyses, this eliminates the small first peak seen in the MB water model radial distribution function which is not observed from analyses of x-ray and neutron scattering experiments of liquid water. Along with this structural change, we investigated how the various thermodynamic properties and anomalies are altered, and we also investigated how these changes alter TPT and IET modeled on the real parametrization of the rose water model.

The temperature dependence of the number density of the rose water model at two constant pressures is shown in Fig. 13. The simulation results indicate a behavior similar to the rose water model with the MB parametrization at the same constant pressures, with magnitudes ranging between 0.2 and 1.1 throughout the reported temperature range. A density

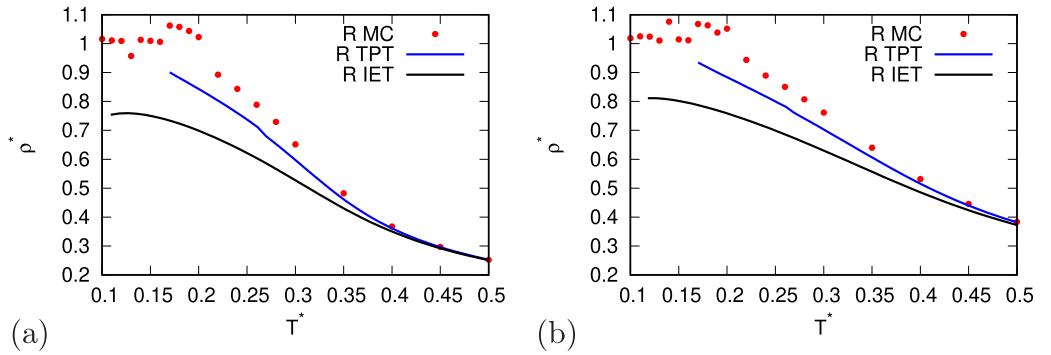

FIG. 13. The rose water model with the real parametrization has a maximum in density in the liquid-to-supercooled region that is only about 10% greater than the density of solid form at temperatures at constant pressure (a) $p^* = 0.12$ and (b) $p^* = 0.19$. The red points show results from MC simulations, while the blue line shows results from TPT and the black line shows results from IET.

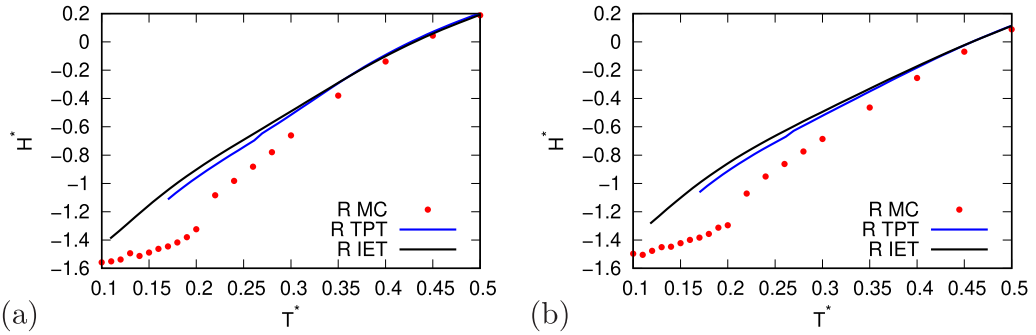

FIG. 14. The real parametrization of the rose water model has a lower excess enthalpy than the MB water model. Shown here is the excess enthalpy as a function of temperature at constant pressure (a) $p^* = 0.12$ and (b) $p^* = 0.19$. The red points are results from MC simulations, while the blue and black lines are results from TPT and IET, respectively.

maximum looks to appear just below $T^* = 0.2$, though it is possible this is in the supercooled liquid region at these target pressures. Expectedly, the number density increases throughout this temperature series when simulations are performed at a higher constant pressure.

Of the analytical theories, TPT is more successful than IET at predicting the magnitude of the simulated densities of the rose water model. The agreement between TPT and the rose water model is strong at temperatures at and above 0.3, but the densities increasingly deviate as the temperature lowers. Note that due to parameter convergence of the applied algorithm, TPT is limited to temperatures above 0.17 in this and other property analyses. TPT is unable to reproduce a density maximum, which is not unexpected given the similar inability seen previously. Interestingly, IET does predict a density maximum at a marginally lower temperature than where one looks to exist in the rose water model. This agreement is tempered by the density being approximately 30% lower than the MC simulations. The poor agreement for the magnitude of the densities at low temperatures is expected given the lack of structure in IET, seen in the previous radial distribution function analyses.

The excess enthalpy and entropy as a function of temperature for the rose water model with the real parametrization are shown in Figs. 14 and 15. While the shapes of the trend are similar to that seen in the MB water model comparisons, the values remain lower for enthalpy and entropy throughout the temperature range at these same constant pressures. Where values would shift from negative to positive above a temperature of 0.3 in the MB water model comparisons, the excess enthalpy does not reach positive values until temperatures higher than 0.4. The reason for this shift comes from the less repulsive nature of the interaction potential, as seen in the lack of red away from the LJ contact surface in Fig. 1(b). The other notable feature in this property is the change in curvature below temperatures of 0.2. This is likely a product of the expected phase transition in this temperature region at the chosen constant pressures.

As with the previous comparisons to MB water and its rose water model parametrization, the agreement between TPT and IET with MC simulations is good primarily at high temperatures. Both TPT and IET have notably higher excess enthalpies at temperatures below 0.3. The higher enthalpy values are expected given the lack of structure depicted by these methods. Of the two methods TPT is closer to the rose water model simulation results, but this improvement is quite small. Overall, the agreement between TPT and IET with the real parametrization of the rose water model is poorer, as these methods show larger differences in excess enthalpy in the low temperature region.

The temperature dependence of the excess heat capacity of the real parametrization of the rose water model, shown in Fig. 16 at two constant pressures, shows similar behavior to the MB parametrization. There are again two notable maxima, with the taller peak indicative of a solid to liquid phase transition, and the lower and broader peak at higher temperature

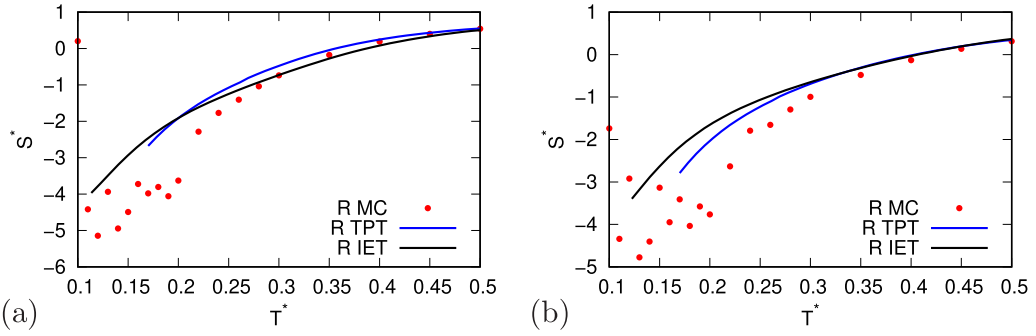

FIG. 15. The real parametrization of the rose water model has a higher excess entropy than the MB water model. Shown here is the excess entropy as a function of temperature at constant pressure (a) $p^* = 0.12$ and (b) $p^* = 0.19$. The red points are results from MC simulations, while the blue and black lines are results from TPT and IET, respectively.

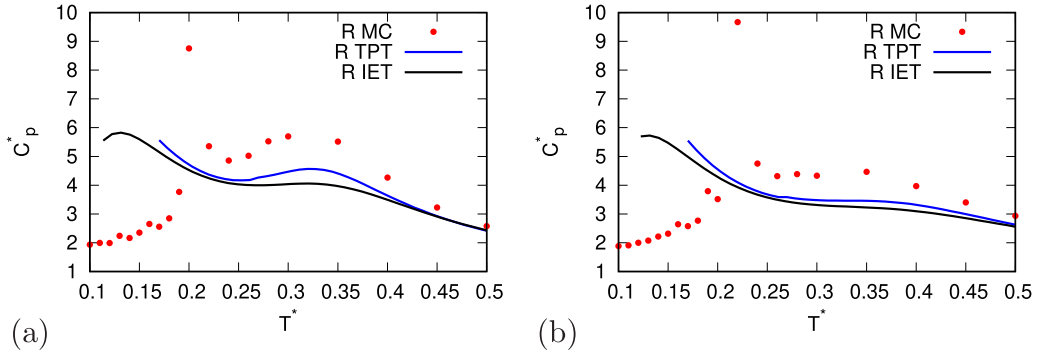

FIG. 16. TPT and IET show similar trends to rose water for the excess heat capacity as function of temperature at constant pressure (a) $p^* = 0.12$ and (b) $p^* = 0.19$. The red points are results from MC simulations, while the blue and black lines are results from TPT and IET, respectively.

corresponding to the dynamical behavior of strong hydrogen bonding contacts. The key difference is the shift in the peak maxima to higher temperatures. This increase is consistent with the observed lower excess enthalpy and generally more attractive nature of the model.

The comparisons to TPT and IET set the rose water model results in Fig. 16 apart from those seen in Fig. 10. At high temperature both TPT and IET have a low C_p^* like the MC simulations, but the agreement degrades as the temperature decreases. Both TPT and IET are unable to reproduce the drop in the C_p^* at very low temperatures, and this is unsurprising given their inability to reproduce solid phase properties. However, at intermediate temperatures and low pressure both TPT and IET reproduce a maximum just above 0.3, right where the MC simulations exhibit a similar maximum. While the height of this maximum is lower than that seen in the MC simulations, this is behavior not observed in the MB model comparisons. As the pressure increases to 0.19, the magnitude of this peak is reduced to the point that the maximum at low pressure becomes a saddle point at high pressure, similar to the behavior of the MC simulations. Both TPT and IET have lower C_p^* values than the MC simulations, but TPT is a bit closer to the simulation results in most cases, indicating that it is a bit more successful at matching simulation behavior.

Figure 17 shows the coefficient of thermal expansion for the rose water model with the real parametrization as function of temperature at two different pressures. As with the MB parametrization, a peak is observed at temperatures above 0.25 and the coefficient gradually approaches a value of $1/T^*$ at very high temperatures. As the temperature decreases, the coefficient of thermal expansion decreases, though there is an unexpectedly anomalous spike similar to that seen in the temperature dependence of C_p^* in Fig. 16. In many respects the properties behave quite similarly as the location and magnitude of the peaks in these plots are near the same values, such as the main broad peak around a temperature of 0.32. This is a higher temperature than the expansion coefficient peak of the MB parametrization, again a consequence of this real parametrization being less repulsive.

TPT is generally quite successful at predicting the coefficient of thermal expansion for this rose water model. The values are the same at high temperatures and near a temperature of 0.25, and it only modestly underpredicts the magnitude of the peak maximum at both of the target pressures. This is notably better agreement than that seen for the MB water parametrization in Fig. 10. At low temperature, both TPT and IET fail to reproduce the expansion coefficient seen in MC simulations. IET does actually drop to a negative value at low temperature, but it tends to underpredict the magnitude of the coefficient of thermal expansion moreso than TPT at all other temperatures.

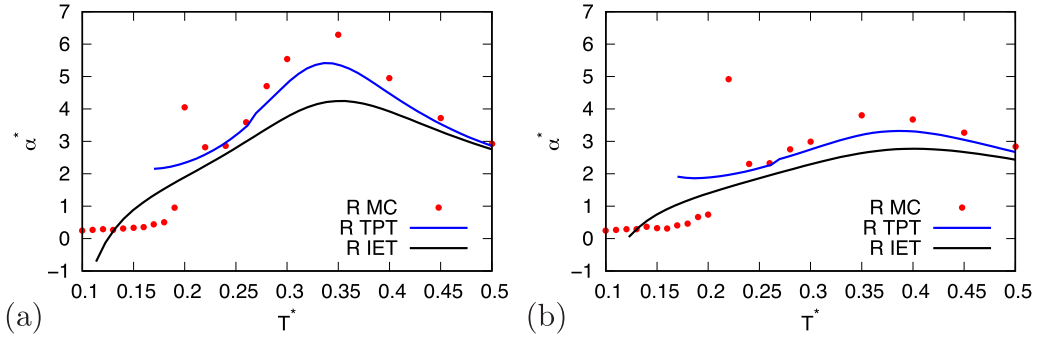

FIG. 17. Simulations of the rose water model with the real parametrization show a familiar peak in the coefficient of thermal expansion, though the shift to negative values near the apparent solid to liquid phase transition temperature is not visible at constant pressures of (a) $p^* = 0.12$ and (b) $p^* = 0.19$. The red points are results from MC simulations, while the blue and black lines are results from TPT and IET, respectively.

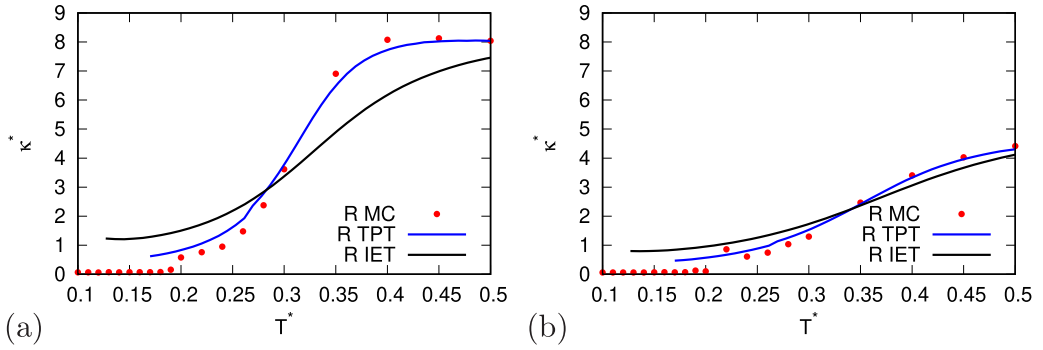

FIG. 18. TPT is able to predict the isothermal compressibility of the rose water model as function of temperature at constant pressures of (a) $p^* = 0.12$ and (b) $p^* = 0.19$. The red points are results from MC simulations, while the blue and black lines are results from TPT and IET, respectively.

Figure 18 shows the temperature dependence of the isothermal compressibility at two constant pressures. In the solid phase at low temperature rose water is quite incompressible, but above the expected melting temperature at these pressures the compressibility rapidly increases and asymptotically approaches a value of $1/p^*$. This observed behavior is similar to that seen with the MB parametrization model, only shifted to higher temperatures as seen for other thermodynamic parameters. The primary point of note is how well TPT reproduces the compressibility at temperatures above 0.2 for both pressures. TPT captures the overall change in the compressibility better than IET.

The general quality of agreement of TPT, and to a lesser extent IET, with the real parametrization of the rose water model is greater than that seen with the MB parametrization and MB water model. This improvement is a reflection of the increased promiscuity of the HB interaction in the rose water model. The rose water model is more accepting of bent hydrogen bonds, and this is more compatible with the approximations used for these strong interactions in the analytical theories. This agreement is directly seen in the structure via the radial distribution functions, and this carries over to nearly all the investigated thermodynamic properties.

V. CONCLUSIONS

We have applied two statistical-mechanical theories developed for associated fluids by Wertheim, TPT and IET, to the rose model of water and compared results to those of the Mercedes-Benz model of water. Both of these theories have previously been shown to capture the volume anomalies of pure water and the thermal anomalies of nonpolar solvation, and we observe similar behavior in their ability to capture such features with the two-dimensional rose water model, particularly when using a parametrization that better mimics the behavior of pure water. Of these two theories, IET is somewhat more computationally demanding than TPT, but both are orders of magnitude more efficient than Monte Carlo simulations. Both theories qualitatively reproduce the temperature trends of key thermodynamic properties like molar volume, isothermal compressibility, thermal expansion coefficient, and heat capacity. This reproduction becomes quantitative agreement at high temperatures, where the orientational averaging approximation is less problematic. This agreement carries over to less rigidly structured fluids, and it is reflected in the increased quality of structural and thermodynamic property predictions for the rose water model over the Mercedes-Benz water model and parametrization sets.

ACKNOWLEDGMENTS

The financial support of the Slovenian Research Agency through Grant No. P1-0201 as well as to Projects No. J7-1816, No. J1-1708, No. N1-0186, and No. L2-3161 is acknowledged, as well as National Institutes for Health RM1 Award No. RM1GM135136.

[1] F. Franks, *Water: A Matrix of Life* (Royal Society of Chemistry, Cambridge, UK, 2000).
[2] B. Guillot, J. Mol. Liq. **101**, 219 (2002).
[3] H. J. C. Berendsen, J. P. M. Postma, W. F. van Gunsteren, and J. Hermans, *Interaction Models for Water in Relation to Protein Hydration. Intermolecular Forces* (Reidel Publishing Company, Dordrecht, 1981).
[4] W. L. Jorgensen, J. Chandrasekhar, J. D. Madura, R. W. Impley, and M. L. Klein, J. Chem. Phys. **79**, 926 (1983).
[5] H. W. Horn, W. C. Swope, J. W. Pitera, J. D. Madura, T. J. Dick, G. L. Hura, and T. Head-Gordon, J. Chem. Phys. **120**, 9665 (2004).
[6] J. L. F. Abascal and C. Vega, J. Chem. Phys. **123**, 234505 (2005).
[7] M. W. Mahoney and W. L. Jorgensen, J. Chem. Phys. **112**, 8910 (2000).
[8] P. Ren and J. W. Ponder, J. Phys. Chem. B **107**, 5933 (2003).
[9] W. Bol, Mol. Phys. **45**, 605 (1982).
[10] W. R. Smith and I. Nezbeda, J. Chem. Phys. **81**, 3694 (1984).
[11] I. Nezbeda, J. Mol. Liq. **73-74**, 317 (1997).
[12] A. Ben-Naim, J. Chem. Phys. **54**, 3682 (1971).
[13] K. A. T. Silverstein, A. D. J. Haymet, and K. A. Dill, J. Am. Chem. Soc. **120**, 3166 (1998).

[14] G. Andaloro and R. M. Sperandeo–Mineo, Eur. J. Phys. **11**, 275 (1990).
[15] K. A. T. Silverstein, K. A. Dill, and A. D. J. Haymet, Fluid Phase Equilib. **120**, 3166 (1998).
[16] N. T. Southall and K. A. Dill, J. Phys. Chem. B **104**, 1326 (2000).
[17] K. A. T. Silverstein, K. A. Dill, and A. D. J. Haymet, J. Chem. Phys. **114**, 6303 (2001).
[18] B. Hribar Lee, N. T. Southall, V. Vlachy, and K. A. Dill, J. Am. Chem. Soc. **124**, 12302 (2002).
[19] C. L. Dias, T. Hynninen, T. Ala–Nissila, A. S. Foster, and M. Karttunen, J. Chem. Phys. **134**, 065106 (2011).
[20] T. Urbič, V. Vlachy, Y. V. Kalyuzhnyi, N. T. Southall, and K. A. Dill, J. Chem. Phys. **112**, 2843 (2000).
[21] T. Urbič, V. Vlachy, Y. V. Kalyuzhnyi, N. T. Southall, and K. A. Dill, J. Chem. Phys. **116**, 723 (2002).
[22] T. Urbič, V. Vlachy, Y. V. Kalyuzhnyi, and K. A. Dill, J. Chem. Phys. **118**, 5516 (2003).
[23] T. Urbic, V. Vlachy, O. Pizio, and K. A. Dill, J. Mol. Liq. **112**, 71 (2004).
[24] T. Urbic, V. Vlachy, Y. V. Kalyuzhnyi, and K. A. Dill, J. Chem. Phys. **127**, 174511 (2007).
[25] T. Urbic, V. Vlachy, Y. V. Kalyuzhnyi, and K. A. Dill, J. Chem. Phys. **127**, 174505 (2007).
[26] T. Urbic and M. F. Holovko, J. Chem. Phys. **135**, 134706 (2011).
[27] T. Urbic and K. A. Dill, J. Chem. Phys. **132**, 224507 (2010).
[28] T. Urbic, Phys. Rev. E **96**, 032122 (2017).
[29] T. Urbic and T. Mohoric, J. Chem. Phys. **146**, 094505 (2017).
[30] P. Ogrin and T. Urbic, J. Mol. Liq. **327**, 114880 (2021).
[31] P. Ogrin and T. Urbic, J. Mol. Liq. **330**, 115671 (2021).
[32] P. Ogrin and T. Urbic, J. Mol. Liq. **337**, 116453 (2021).
[33] C. H. Williamson, J. R. Hall, and C. J. Fennell, J. Mol. Liq. **228**, 11 (2017).
[34] M. S. Wertheim, J. Stat. Phys. **42**, 459 (1986).
[35] M. S. Wertheim, J. Chem. Phys. **87**, 7323 (1987).
[36] E. A. Muller and K. E. Gubbins, in *IUPAC Volume on Equations of State for Fluids and Fluid Mixtures*, edited by J. V. Sengers, M. B. Ewing, R. F. Kayser, and C. J. Peters (Blackwell Scientific, Hoboken, NJ, 1999).
[37] Y. V. Kalyuzhnyi and P. T. Cummings, in *IUPAC Volume on Equations of State for Fluids and Fluid Mixtures*, edited by J. V. Sengers, M. B. Ewing, R. F. Kayser, and C. J. Peters (Blackwell Scientific, Hoboken, NJ, 1999).
[38] I. Nezbeda, J. Kolafa, and Y. V. Kalyuzhnyi, Mol. Phys. **68**, 143 (1989).
[39] I. Nezbeda and G. A. Iglezias–Silva, Mol. Phys. **69**, 767 (1990).
[40] J. Chang and S. I. Sandler, J. Chem. Phys. **102**, 437 (1995).
[41] E. V. Vakarin, Y. Ja. Duda, and M. F. Holovko, Mol. Phys. **90**, 611 (1997).
[42] J. D. Talman, J. Comput. Phys. **29**, 35 (1978).
[43] M. S. Wertheim, J. Chem. Phys. **88**, 1145 (1988).
[44] J. A. Barker and D. Henderson, J. Chem. Phys. **47**, 2856 (1967).
[45] J. A. Barker and D. Henderson, J. Chem. Phys. **47**, 4714 (1967).
[46] J. A. Barker and D. Henderson, Rev. Mod. Phys. **48**, 587 (1976).
[47] O. H. Scalise, G. J. Zarrafoicoechea, L. E. Gonzalez, and M. Silbert, Mol. Phys. **93**, 751 (1998).
[48] D. J. Gonzalez, L. E. Gonzalez, and M. Silbert, Mol. Phys. **74**, 613 (1991).
[49] J. P. Hansen and I. R. McDonald, *Theory of Simple Liquids* (Academic Press, London, 1986).